Non-parametric stress field estimation for history dependent materials: Application to ductile material exhibiting Piobert-Lüders localization bands

Raphaël Langlois, Michel Coret, Julien Réthoré

Received: Added at production | Revised: Added at production | Accepted: Added at production

DOI: xxx/xxxx

ARTICLE TYPE

Non-parametric stress field estimation for history dependent materials: Application to ductile material exhibiting Piobert–Lüders localization bands

R. Langlois | M. Coret | J. Réthoré*

[1]Research Institute in Civil Engineering and Mechanics, GeM, Centrale Nantes, Universté de Nantes, CNRS, UMR 6183, Nantes, France

Correspondence
* Julien Réthoré, Research Institute in Civil Engineering and Mechanics, GeM, Centrale Nantes, 44300 Nantes, France Email: julien.rethore@ec-nantes.fr

Abstract

Estimating stress in statically undetermined tests remains an issue in experimental mechanics. Most estimation methods rely on the *a priori* choice of a behavior equation leading to an unavoidable model bias. Recently efforts have been made to propose methods circumventing the parametric description to constitutive model. In particular, Leygue et al. (2018) proposed a new paradigm called Data-Driven Identification (DDI). An extension of Leygue's method to history dependent materials is proposed in this paper. The formulation of the problem and its resolution are presented with emphasis on boundary conditions. The method is tested on real experimental data where the elasto-plastic material is subjected to the formation of Piobert-Lüders bands. We finally show that the DDI allows to obtain balanced fields that are closer (more consistent) to the field measurements than the fields obtained by parametric identification strategies, even more in the presence of strain localization bands whose kinematics are usually not described by a standard constitutive model.

KEYWORDS:
Data-Driven Identification; Digital Image Correlation; Plasticity; Piobert–Lüders band;

1 | INTRODUCTION

Stress estimation during statically undetermined tests remains an open issue as no measurement can be made to directly infer the stress, unlike strains that can be estimated using full-field kinematic measurement methods [1, 2]. One way of assessing stresses is to identify the parameters of a constitutive equation using inverse methods (Finite Element Model Updating (FEMU) , Virtual Field Method (VFM), Constitutive Equation Gap Method (CEGM), Equilibrium Gap Method (EGM)...) [3]. These methods

[0]**Abbreviations:** DIC, Digital Image Correlation; DDI, Data-Driven Identification; RoI, Region of Interest

allow to compute the stress using the identified parameters of the pre-supposed constitutive equation in complex cases [4, 5, 6, 7, 8]. However an *a priori* choice of a constitutive equation has to be made which may lead to a significant modeling error and does not allow to reach uncertainty levels of the measurement [9]. Neggers *et al.* [10] propose a(n) Integrated-DIC method (similar to FEMU) where various enrichments (adding material parameters) of a constitutive model are compared by analyzing the identification residual and the sensitivity fields. Enriching the description does improve the identification residual, but a significant gap with respect to the measurements (higher in magnitude compared to the measurements uncertainty) remains and no systematic method for selecting the added material parameter is proposed.

Recently a number of contributions [11, 12, 13, 14, 15, 16] have addressed these issues. In [11, 12], the authors use acceleration field measurements to compute stress directly from the mechanical balance of momentum. This approach does remove all assumptions linked to the choice of a constitutive equation, but it has only been used on 1D experiment under purely inertial or vibratory loading making this method inadequate for quasi-static experiments. [14, 13] propose methods based on an assumption that the principal direction of stress and strain (or stress and strain rate) are collinear. But in general (*e.g.* anisotropy, localization,...) a material constitutive relation does not present these properties leading to a significant assumption failing for a large class of materials.

The proposition of [15, 16], coined as Data-Driven Identification (DDI), is based on the new computational paradigm introduced in [17, 18] and may help us solve the issues described above and questions inherent to parametric methods. These methods are based on the relaxation of the constraint of exactly satisfying a constitutive equation. Leygue *et al.* [16] show on synthetic data that a data-driven approach can be used to identify admissible stresses in a structure from full-field kinematic and load cell measurements without any assumption on the form of the relation between the measured strain and the reconstructed stress. They showcased the versatility of the method by testing it on various types of loading conditions (quasi-static and dynamic) and non-linearity sources (hyperelasticity and elasto-plasticity under monotonic loading). The method was applied on real experimental data in [19], where perforated hyperelastic membranes were tested to generate strain and stress states significantly different from an uniaxial experiment. The key outputs of the method are stress fields that balance exactly the applied loads and a discrete description of the explored space of admissible state in the constitutive space $(\boldsymbol{\sigma}, \boldsymbol{\varepsilon})$ (or $(\boldsymbol{\sigma}, \log \boldsymbol{v})$ in [19]).

In the context of history dependent materials, the literature on Data-Driven method is still lacking especially regarding stress estimation. However, on the computational side, attempts have been made to propose frameworks in the case of inelasticity. Ladevèze *et al* [20] and Chinesta *et al* [21] proposed a formalism for elasto-plasticity that still requires an *a priori* knowledge of the internal variables, which does not remove all the drawbacks associated to classical identification approaches. Eggersman *et al.* [22], proposed several formal settings describing inelastic behaviors. The *differential representation* seems well suited for stress estimation from experimental kinematic data as it only requires fundamental quantities of continuum mechanics: it simply consists in describing the material behaviour using strain, stress and a number of their respective time derivatives. This

representation can provide a complete description of the behavior of a material when the number of considered derivatives tends to infinity.

Here we propose an extension of the Data-Driven Identification (DDI) method introduced in [16] to history dependent materials using the *differential representation* but we limit ourselves to first order time derivatives. A consequence of this choice being that long term stress-strain time interaction will not be properly captured by the proposed method but straightforward extensions could be made. The method is illustrated on an experiment on a low-carbon steel sample presenting strain rate localization bands. We limit the application case to 2D analyses (as usual for parametric identification strategy like FEMU) but the proposed strategy could be extended to 3D using Digital Volume Correlation measurements obtained for example from *in-situ* experiments inside a X-ray tomograph. However, DIC measurements from tests using classical loading devices have become a standard in experimental mechanics. Thus presenting the method in this usual configuration is a first but mandatory step before generalizing the method.

The paper is organized as follows: Section 2 introduces the DDI framework [15, 16] and the proposed resolution algorithm. Section 3 presents an experimental application from data acquisition to processing. Then Section 4 analyses the impact of a few algorithmic parameters on the DDI solution. Finally Section 5 compares the output of the DDI method to the output of a classical parametric method (here FEMU) using two indicators to assess the mechanical quality of the estimated response and last, a qualitative analysis of the estimated stress is carried out.

2 | MODEL-FREE IDENTIFICATION FOR HISTORY DEPENDENT MATERIALS

Data-Driven Identification aims at reconstructing the stress state in a structure without making assumptions on the parametric form of the constitutive relation. The price to pay is to have rich databases of measured displacement fields (usually from DIC) as well as imposed forces on the structure (measured by load cell). In the following section, we recall the formulation of the mechanical problem introduced in [15, 16] then, the extension is made to generalize the problem to history dependent materials following the recommendation of [22] and a modification of the resolution strategy proposed in [16] is introduced.

The method is presented under small strain assumption, however, it has been implemented and used in the case of finite strain by using appropriate measures of stress and strain in [19]. The notations relative to the method will also be introduced. All equations are written in a space and time discretized format (such as finite element).

2.1 | Data-Driven Identification, a recall

We consider a loaded 2D structure made of a deformable material, however all the methods presented herein can be extended to 3D. The structure is discretized using a finite element mesh (with N_e elements and N_n nodes) and is submitted to a net force F_{mes}. Nodal displacements $\mathbf{u}_k$ and forces are known at every time step $j \in [1, N_t]$ (N_t being the number of time steps).

2.1.1 | Data, discretization and norm definitions

From the experiment, the following data are considered to be available for each time step j:

- $\mathbf{u}_k^j$: the displacement measured at every node k of the mesh;
- $\mathbf{B}_{ek}^j$: an operator, calculated from the geometry and mesh connectivity allowing to compute the strain tensor at every integration point e:

$$\boldsymbol{\varepsilon}_e^j = \sum_{k=1}^{N_n} \mathbf{B}_{ek}^j \cdot \mathbf{u}_k^j, \tag{1}$$

- F_{mes}^j: the net force of the nodal forces on the boundary ∂F

$$F_{mes}^j = h \sum_k \mathbf{f}_k^j \quad \forall k \in \partial F, \tag{2}$$

with h the thickness of the structure, supposed to be constant and ∂F the discretized physical boundaries on which Neumann conditions are measured (imposed later on).

A symmetric positive definite fourth-order tensor $\mathbb{C}$ is introduced. This tensor allows us to sum quantities of different units (strains and stresses in our case). Following [17] and [16], we introduce the $\| \bullet \|_{\mathbb{C}}$ norm:

$$\|(A, B)\|_{\mathbb{C}}^2 = \frac{1}{2}(A : \mathbb{C} : A + B : \mathbb{C}^{-1} : B)\,, \tag{3}$$

with A and B two second-order tensors.

As the problem of finding the stresses without a constitutive equation is ill-posed, a key point of the method is the introduction of an unknown set of points $(\boldsymbol{\varepsilon}^*, \boldsymbol{\sigma}^*)$, clustering the set of given strains and searched stresses $(\boldsymbol{\varepsilon}_e^j, \boldsymbol{\sigma}_e^j)$ that are close (within the $\| \bullet \|_{\mathbb{C}}$ norm sense). The set $(\boldsymbol{\varepsilon}^*, \boldsymbol{\sigma}^*)$, of cardinal N^* can be viewed as a discretization of the admissible stress-strain manifold. This is the reason why we call them *material states*. We also define the number N_l of local states $(\boldsymbol{\varepsilon}_e^j, \boldsymbol{\sigma}_e^j)$ as the number of elements multiplied by the number of time steps ($N_l = N_e \times N_t$).

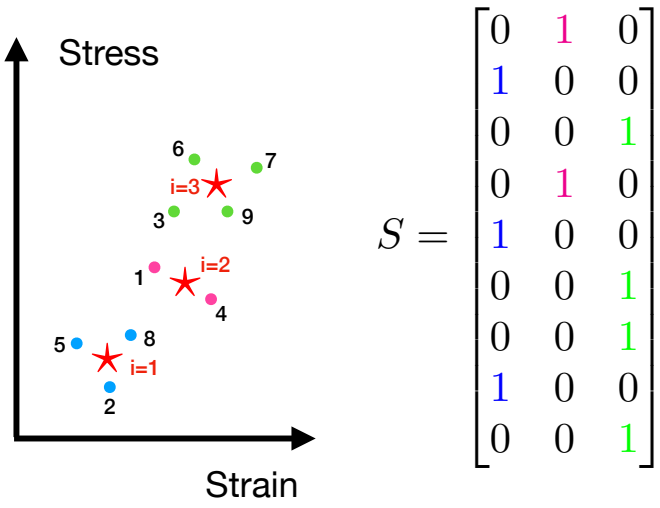

Figure 1 Example of a selection matrix S, the red stars are the material states and the colored dots the local states (in 1D).

2.1.2 | Data-Driven Identification in elasticity

In the context of non-linear elasticity (including monotonous plasticity) or more generally when the local stress-strain relation remains bijective (*i.e.* non-linear behavior with no strain rate effect) [15], the problem is written as a global minimization problem:

$$\min_{\boldsymbol{\sigma}_e, \boldsymbol{\sigma}^*, \boldsymbol{\varepsilon}^*, \mathcal{S}} \frac{1}{2} \sum_j \sum_e w_e^j \| \boldsymbol{\varepsilon}_e^j - \mathcal{S}_e^j \boldsymbol{\varepsilon}^*, \boldsymbol{\sigma}_e^j - \mathcal{S}_e^j \boldsymbol{\sigma}^* \|_{\mathbb{C}}^2, \tag{4}$$

under the constraint of mechanical equilibrium written in a discrete form:

$$\sum_{e=1}^{N_e} w_e^j \mathbf{B}_{ek}^{j\,T} \boldsymbol{\sigma}_e^j = \mathbf{f}_k^j. \tag{5}$$

$\sum_e$ stands for the sum over the domain (or over all integration points), $\sum_t$ stands for the sum over all time steps, w_e^j is the weight of integration point e and $\mathcal{S}^j$ a selection matrix that encodes the mapping between material states $(\boldsymbol{\varepsilon}^*, \boldsymbol{\sigma}^*)$ and local states $(\boldsymbol{\varepsilon}_e^j, \boldsymbol{\sigma}_e^j)$. $\mathcal{S}_e^j$ refers to line e of the matrix $\mathcal{S}^j$. $\mathcal{S}^j$ is a N^* by N_e matrix with each line having a single non zero entry ($\|\mathcal{S}_e^j\|_2 = 1$) that projects the material states associated to each element into the physical space, *i.e.* associate a point in the physical space to a single point in the material state space.

Figure 1 shows an example of a selection matrix in the case of uni-dimensional strain and stress data set.

The strain compatibility is verified as local strains $\boldsymbol{\varepsilon}_e^j$ are derived directly from measured displacements. The use of Equation (4) allows to close the problem, the $\| \bullet \|_{\mathbb{C}}$ norm is used to iteratively update the material and mechanical states and ensures that the spread (standard deviation) of mechanical states w.r.t. the material states is minimized.

The resolution of this particular problem is extensively discussed in [15, 16, 23]. A few points should be highlighted: (i) the equilibrium Equation (5) is imposed during resolution by using Lagrange multipliers, (ii) finding the selection matrix $\mathcal{S}$ has a high computational cost involved by multiple loops through the data, (iii) the formulation above is a heuristic method which does not guarantee to obtain the global minimum of the problem.

2.1.3 | Data-Driven Identification of a correction to a constitutive equation

In the following, we recall a second method proposed in [16] where the initialization is based on the identification of a constitutive model made by Finite Element Model Updating (FEMU) approach under prescribed loading. The idea being to initialize the stresses, other methods of identification would also work. This initial stress field is noted $\bar{\boldsymbol{\sigma}}_e$ and satisfies the equilibrium equation. The FEMU approach considered in the following uses load control FE simulations. The proposed modification of the DDI problem (Equations (4) and (5)) is then straightforward. The problem consists in finding the true stress field as a correction $\tilde{\boldsymbol{\sigma}}_e$ of the initial one. We introduce:

$$\boldsymbol{\sigma}_e^j = \tilde{\boldsymbol{\sigma}}_e^j + \bar{\boldsymbol{\sigma}}_e^j. \tag{6}$$

As the initial solution balances the external load *exactly*, the correction can be of two forms, (1) a self-balanced stress field or (2) a stress field balancing a force distribution whose resultant is null on the considered boundaries ∂F. These self-balanced corrections can be searched on a basis of admissible stress fields [16]. Let us suppose that this basis $\mathbb{L} = \{\mathbf{L}_e\}_{e=1\dots N_e}$ of $N_{\mathbb{L}}$ vectors (where $\mathbf{L}_e$ is a 3 by $N_{\mathbb{L}}$ matrix, $\tilde{\boldsymbol{\sigma}}_e^j$ having 3 components in 2D, collecting all possible combinations of self-balanced stress at element e) is known, the stress field is written as:

$$\boldsymbol{\sigma}_e^j = \mathbf{L}_e \mathbf{P}^j + \bar{\boldsymbol{\sigma}}_e^j, \tag{7}$$

where $\mathbb{P} = \{\mathbf{P}^j\}_{j=1\dots N_t}$ ($\mathbf{P}^j$ is a vector of $N_{\mathbb{L}}$ components collecting the amplitudes of the correction basis at time j) are the amplitudes associated to each vector of the basis. The generation of $\mathbb{L}$ is detailed in the next section. Identifying the stress field now consists in finding $\mathbb{P}$ minimizing Equation (4).

This formulation allows to completely relax the balance of momentum constraint (Equation (5)) on the minimization problem as any stress field resulting from Equation (7) satisfies this constraint.

2.1.4 | Self-balanced basis computation

From here, small strain assumption is adopted, leading to two simplifications: $w_e^j = w_e$ and $\mathbf{B}_{ek}^j = \mathbf{B}_{ek}$.

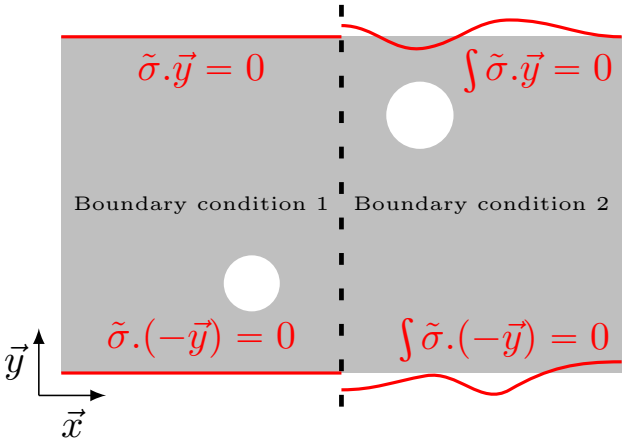

Figure 2 Difference between the type of boundary condition treatment illustrated on the geometry used later on. The load profile on the right side is not representative of the actual internal forces carried by the stress correction on ∂F.

The internal force vector resulting from the correction field can be written as,

$$\sum_{e=1}^{M} w_e \mathbf{B}_{ek}{}^T \tilde{\boldsymbol{\sigma}}_e^j = \mathbf{f}_k^{int} = \mathbf{0}, \quad \text{in the volume.} \tag{8}$$

The corrected stress field also has to verify the equilibrium on the boundaries ∂F (the discretized physical boundaries on which Neumann conditions are imposed). First, we can consider a regular type of condition where the correction has no influence on each node of the boundaries. This condition enforces a zero correction of the nodal force $\mathbf{f}_k^{int}$ at each node of ∂F. This condition is noted as *strong* or *boundary condition 1* in the following. This is written:

$$\mathbf{f}_k^{int} = \mathbf{0}, \quad \forall k \in \partial F. \tag{9}$$

Another possibility is to conserve the net force on the boundary ∂F. This non regular type condition better corresponds to a boundary on which we measure the net force (for example the section at the end of a specimen). In this case, called *weak condition* or *boundary condition 2*, the corrected stress field has to verify:

$$\sum_k \mathbf{f}_k^{int} = \mathbf{0}, \quad \forall k \in \partial F. \tag{10}$$

The difference between the two types of boundary condition treatment is showcased on fig. 2. The conditions are written in classical continuum mechanics form.

Then, we have to generate the basis $\mathbb{L}$ as defined previously. $\mathbb{L}$ (resp. $\hat{\mathbb{L}}$) is the kernel (nullspace) of the divergence operator $\mathcal{B}^T$ (resp. $\hat{\mathcal{B}}^T$) defined by Equations (5) and (9) (resp. Equations (5) and (10)):

$$\mathbb{L} = \ker(\mathcal{B}^T) \quad \text{or} \quad \hat{\mathbb{L}} = \ker(\hat{\mathcal{B}}^T). \tag{11}$$

Remark

For a mesh consisting in triangular elements using first order interpolation and one integration point, $\mathbb{L}$ is composed of $N_{\mathbb{L}} = 3N_e - 2N_n$ vectors of size $(3N_e \times 1)$. In the case of the modified divergence operator $\hat{\mathcal{B}}^T$, the number $\hat{N}_{\mathbb{L}}$ of vector in $\hat{\mathbb{L}}$ varies with the number of nodes on the boundaries where the condition is relaxed but this condition $\hat{N}_{\mathbb{L}} \geq N_{\mathbb{L}}$ is always verified.

2.2 | Extension of the method to inelastic behaviours

As stated previously, the proposed formulation of DDI are not suitable for history dependent materials.

2.2.1 | Choice of the representation

Following the recommendation of Eggersmann *et al.* [22], we use a *differential representation* to take history effects into account. The number of time derivatives taken into account might impact the accuracy of the stress for highly time dependent behaviors, however in the current work, we propose to limit the enrichment of the constitutive space to the first order time derivative. The constitutive space in which the solution is searched for becomes: $(\boldsymbol{\varepsilon}, \dot{\boldsymbol{\varepsilon}}, \boldsymbol{\sigma}, \dot{\boldsymbol{\sigma}})$, as the rates are estimated using finite differences, we propose to directly use stress and strain values at previous time to enrich the description. Meaning that the stress identified at time j will depend on: (i) strain at time j, (ii) stresses and strains at time $j-1$. As a consequence of the enrichment, the material states can no longer be limited to the simple set $(\boldsymbol{\varepsilon}^*, \boldsymbol{\sigma}^*)$. From here they are defined as $(\boldsymbol{\varepsilon}^*, \boldsymbol{\varepsilon}^{**}, \boldsymbol{\sigma}^*, \boldsymbol{\sigma}^{**})$, where $\bullet^*$ are related to the current state and $\bullet^{**}$ to the former state.

Issues of none uniqueness of the stress given its history, that may arise in a classical forward problem, may not appear here because the problem solved is not a mechanical problem but a statistical one (finding the stress, strain and their rate of change minimizing the spread around the material points) constrained by the mechanical equilibrium (both in the bulk and on the boundaries), the measured strain and load increments.

2.2.2 | Problem statement

Using the new constitutive space and the decomposition of stress in Equation (7), the minimization problem becomes:

$$\begin{aligned} &\min_{\substack{\mathbb{P},\boldsymbol{\varepsilon}^*,\boldsymbol{\varepsilon}^{**},\\ \boldsymbol{\sigma}^*,\boldsymbol{\sigma}^{**},\mathcal{S}}} \Psi(\mathbb{P}, \boldsymbol{\varepsilon}, \boldsymbol{\varepsilon}^*, \boldsymbol{\varepsilon}^{**}, \boldsymbol{\sigma}^*, \boldsymbol{\sigma}^{**}, \mathcal{S}), \\ \text{with} \quad &\Psi = \frac{1}{2}\sum_{j=2}^{N_t}\sum_{e=1}^{N_e} p_e \|\boldsymbol{\varepsilon}_e^j - \mathcal{S}_e^j\boldsymbol{\varepsilon}^*, \mathbf{L}_e\mathbf{P}^j + \bar{\boldsymbol{\sigma}}_e^j - \mathcal{S}_e^j\boldsymbol{\sigma}^*\|_{\mathbb{C}}^2 \\ &\qquad + p_e \|\boldsymbol{\varepsilon}_e^{j-1} - \mathcal{S}_e^j\boldsymbol{\varepsilon}^{**}, \mathbf{L}_e\mathbf{P}^{j-1} + \bar{\boldsymbol{\sigma}}_e^{j-1} - \mathcal{S}_e^j\boldsymbol{\sigma}^{**}\|_{\mathbb{C}}^2, \end{aligned} \tag{12}$$

p_e being an integration weight for element e the effect of which will analyse the effect in the section 4.

Taking all possible variations of Ψ leads to the following equations set:

$$\delta\boldsymbol{\varepsilon}_i^{**} \Rightarrow \quad \sum_{j=1}^{N_t-1} \sum_{e/S_{ei}^{j+1}=1} p_e \mathbb{C} : (\boldsymbol{\varepsilon}_e^j - S_{ei}^{j+1}\boldsymbol{\varepsilon}_i^{**}) = 0 \quad \forall i, \tag{13}$$

$$\delta\boldsymbol{\varepsilon}_i^{*} \Rightarrow \quad \sum_{j=2}^{N_t} \sum_{e/S_{ei}^{j}=1} p_e \mathbb{C} : (\boldsymbol{\varepsilon}_e^j - S_{ei}^{j}\boldsymbol{\varepsilon}_i^{*}) = 0 \quad \forall i, \tag{14}$$

$$\delta\boldsymbol{\sigma}_i^{**} \Rightarrow \quad \sum_{j=1}^{N_t-1} \sum_{e/S_{ei}^{j+1}=1} p_e \mathbb{C}^{-1} : (\bar{\boldsymbol{\sigma}}_e^j + \mathbf{L}_e^j\mathbf{P}^j - S_{ei}^{j+1}\boldsymbol{\sigma}_i^{**}) = 0 \quad \forall i, \tag{15}$$

$$\delta\boldsymbol{\sigma}_i^{*} \Rightarrow \quad \sum_{j=2}^{N_t} \sum_{e/S_{ei}^{j}=1} p_e \mathbb{C}^{-1} : (\bar{\boldsymbol{\sigma}}_e^t + \mathbf{L}_e^j\mathbf{P}^j - S_{ei}^{j}\boldsymbol{\sigma}_i^{*}) = 0 \quad \forall i, \tag{16}$$

$$\text{and} \quad \delta\mathbf{P}^a \Rightarrow \begin{cases} \sum_{e=1}^{N_e} p_e \mathbf{L}_e^T : \mathbb{C}^{-1} : (\bar{\boldsymbol{\sigma}}_e^a + \mathbf{L}_e\mathbf{P}^a - S_e^{a+1}\boldsymbol{\sigma}^{**}) = 0 \quad \text{if } a = 1, \\ \displaystyle\sum_{e=1}^{N_e} p_e \mathbf{L}_e^T : \mathbb{C}^{-1} : \Big((\bar{\boldsymbol{\sigma}}_e^a + \mathbf{L}_e\mathbf{P}^a - S_e^a\boldsymbol{\sigma}^{*}) \\ \qquad\qquad + (\bar{\boldsymbol{\sigma}}_e^a + \mathbf{L}_e\mathbf{P}^a - S_e^{a+1}\boldsymbol{\sigma}^{**})\Big) = 0 \quad \forall a \in [2, N_t - 1], \\ \sum_{e=1}^{N_e} p_e \mathbf{L}_e^T : \mathbb{C}^{-1} : (\bar{\boldsymbol{\sigma}}_e^a + \mathbf{L}_e\mathbf{P}^a - S_e^a\boldsymbol{\sigma}^{*}) = 0 \quad \text{if } a = N_t. \end{cases} \tag{17}$$

The problem is solved using a staggered algorithm (fixed point scheme):

1. initialize $(\boldsymbol{\varepsilon}_i^*, \boldsymbol{\varepsilon}_i^{**}, \boldsymbol{\sigma}_i^*, \boldsymbol{\sigma}_i^{**})$ and $(S^j)_{1\dots N_t}$ by a k-means algorithm on $(\boldsymbol{\varepsilon}_e^j, \boldsymbol{\varepsilon}_e^{j-1}, \bar{\boldsymbol{\sigma}}_e^j, \bar{\boldsymbol{\sigma}}_e^{j-1})_{e=1\dots N_e, j=1\dots N_t}$,
2. update the selection matrices $(S^t)_t$ using Equation (12) (find (S^j) that minimizes Ψ given all other quantities),
3. update material states using Equations (13) to (16),
4. iterate steps 2-3 until convergence of $(S^t)_{1\dots N_t}$,
5. update $\mathbf{P}^j$ using Equation (17),
6. iterate steps 2 through 5 until convergence on $(S^t)_{1\dots N_t}$ and $(\mathbf{P}_j^j)_{j=1\dots N_t}$,

which is equivalent to solving the following problem:

$$\min_{\mathbf{P}} \Big(\min_{\substack{\boldsymbol{\varepsilon}^*, \boldsymbol{\varepsilon}^{**}, \\ \boldsymbol{\sigma}^*, \boldsymbol{\sigma}^{**}, S}} \Psi \Big). \tag{18}$$

This resolution algorithm might not be optimal and could be discussed at greater length, but this is out of the scope of this paper. The resolution strategy adopted is straightforwardly derived from the DDI algorithm [16] taking the constitutive space defined in the previous section.

2.2.3 | Remarks on the resolution

Initializing and updating $\mathcal{S}^j$

The initial coordinates of the clusters are obtained from a k-means algorithm [24, 25]. They are updated during the resolution using the linear systems given by eqs. (13) to (16). After each update a new selection matrix is computed. The new $(\mathcal{S}^j)$ is computed by pairing all the local states with the cluster that minimizes the distance defined in eq. (12) element-wise. This process requires to loop over all the material states once and local states N^* times.

Updating P

From eq. (17), a linear problem in $\mathbf{P}$ arises for each instant j:

$$\sum_e p_e {\mathbf{L}_e}^T : \mathbb{C}^{-1} : \mathbf{L}_e \delta\mathbf{P}^j = -\frac{1}{2} \sum_e p_e {\mathbf{L}_e}^T : \mathbb{C}^{-1} : ((\boldsymbol{\sigma}_e^j - S_e^j \boldsymbol{\sigma}_i^*) + (\boldsymbol{\sigma}_e^j - S_e^{j+1} \boldsymbol{\sigma}_i^{**})) \tag{19}$$

and taking in consideration the edge cases of the eq. (17) for the expression of the right-hand term, can be condensed in the linear system:

$$\mathbf{K}\delta\mathbf{P} = -\mathbf{F}, \tag{20}$$

where $\mathbf{K}$ is a $N_{\mathbb{L}}$ square matrix (or $\hat{N}_{\mathbb{L}}$ square matrix) defined by $K_{lm} = \sum_e p_e {\mathbf{L}_e^l}^T : \mathbb{C}^{-1} : \mathbf{L}_e^m$, with $\mathbf{L}_e^c$ referring to the column c of the matrix $\mathbf{L}_e$.

Number of material states and convergence criteria

1. The number of material states is chosen using the following criterion $20 \leq \frac{N_t \times N_e}{N^*} \leq 100$ as recommended in [26, 27]. Here we chose a value of 80.

2. Two criteria are needed to define the convergence of the selection matrix and the stress correction:

   - for the selection matrix, convergence is reached when $\frac{|\Psi_i - \Psi_{i-1}|}{\Psi_0} \leq 5 \times 10^{-3}$ with the subscript i describing the iteration number and Ψ_0 the first evaluation of the data-driven distance,
   - for the amplitudes of stress correction, convergence is reached when $\max_t \left(\frac{\|\Delta \mathbf{P}_i^t\|_2}{\|\mathbf{P}_i^t\|_2} \right) \leq 5 \times 10^{-2}$.

Adding more "time sensitivity"

For more complex behavior or for a "better" representation, one can straightforwardly modify the proposed norm by adding dependencies on more history (i.e. more time steps in the norm). However, this will increase the size of the phase space and the problem by extension. For instance in the case of third order time derivative, adding terms on $j-2$ and $j-3$. However, issues relating with the time resolution of the input data may come into play when increasing the phase space.

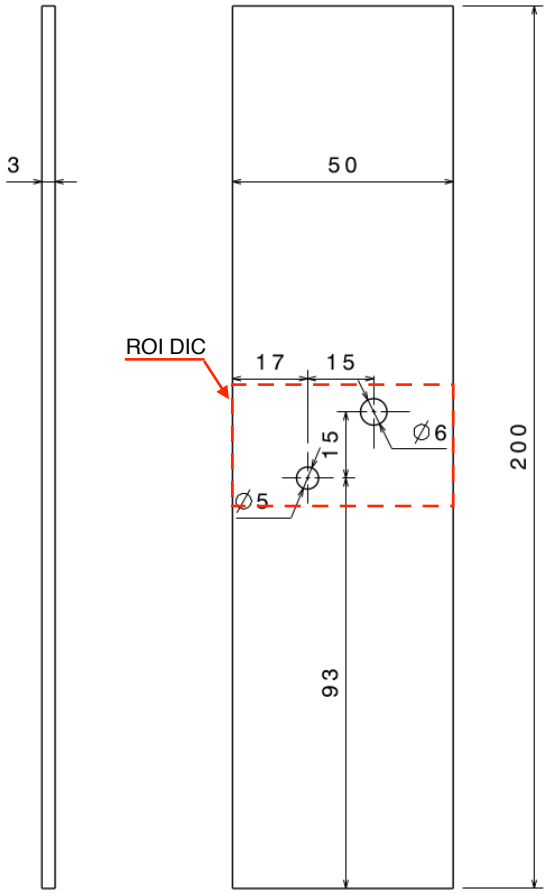

Figure 3 Drawing of the "flounder eyes specimen" geometry (dimensions in mm)

Solution reached

As stated earlier the proposed method does not guarantee that we reach the global minimum. However uncertainties on the identified stress mainly come from the uncertainties on the initial data used (specifically from the kinematic measurement).

3 | METHODS

3.1 | Material and sample geometry

The sample considered in the following is made of S355 steel. It is well established that Piobert–Lüders bands are likely to appear during deformation in this material. A *flounder's eye* geometry is tested (presented in Figure 3). This specimen is a simple rectangular plate of 200 mm × 50 mm × 3 mm dimensions with two holes of diameter 6 mm and 5 mm, drilled near the center. This geometry has no symmetry which leads to relatively complex strain states between holes despite a fairly simple loading.

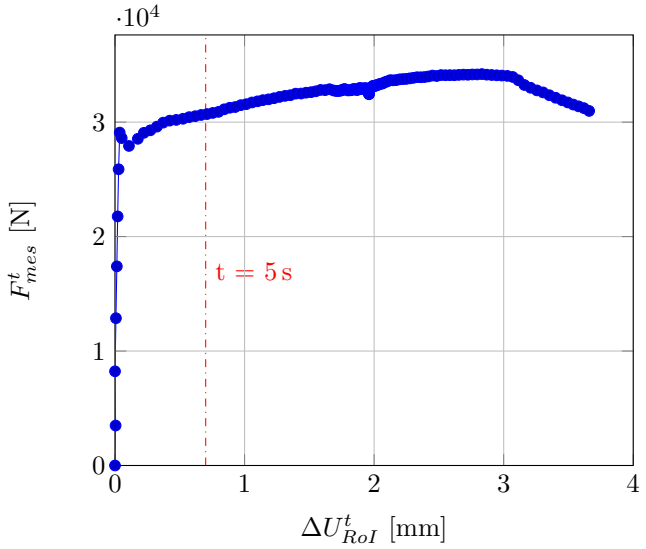

Figure 4 Load versus displacement response of the S355 specimen. Each blue dot corresponds to a measurement time. The displacement is the difference between the mean vertical displacement between the top and bottom edges of the DIC RoI

Camera	Allied Vision Technology Prosilica GT6600
Image resolution	28.8 MPix (6576 Pix by 4384 Pix)
Dynamic Range, Image	8 bits
Acquisition Rate	4 Hz
Telecentric Lens	Opto-Enineering TC 16M 009-F
Magnification	0.64
Field of view	56.2 mm and 37.4 mm
Image scale	1 Pix = 8.55 µm
Patterning Technique	spray paint then airbrush

Table 1 Image acquisition parameters

3.2 | Mechanical test and data acquisition

The sample was loaded in tension with a constant crosshead displacement rate of 0.25 mm/s on a 100 kN MTS hydraulic tensile testing machine, giving the macroscopic response presented in Figure 4 (ΔU^t_{RoI} is the mean value of the vertical displacement between the top and bottom edges of the RoI, measured by DIC).

A black and white speckle pattern is deposited on the specimen, using paint spray and an airbrush. Images of the sample undergoing deformation were taken using a high resolution camera (Allied Vision Technology Prosilica GT6600) 28.8 MPix mounted with a 0.64 magnification telecentric lens (Opto-Enineering TC 16M 009-F) resulting in a physical pixel size of 8.55 µm. The images and applied load F^t_{mes} are acquired synchronously at a constant frequency of 4 Hz. The information is summarized in Table 1.

In the following analysis we will only consider the first twenty measurement points (the first 5 s of the experiment).

DIC Software	Ufreckles [28]
Shape Function	linear triangular finite elements
Matching Criterion	global ZNSSD
Data Processing	$\mathbf{u}$: Tikhonov regularization, cut-off length of 50 Pix
Data Post-Processing	$\boldsymbol{\varepsilon}$: using finite element shape functions, no filtering
	$\dot{\boldsymbol{\varepsilon}}$: finite differences in time, no filtering

Table 2 DIC parameters

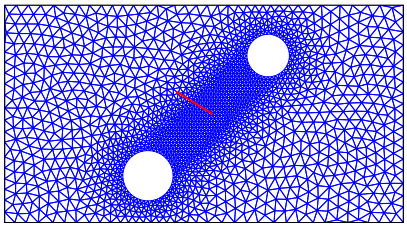

(a) DIC mesh, the red line is used in the result section

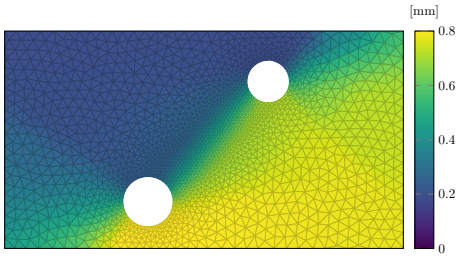

(b) Example of a displacement field (magnitude)

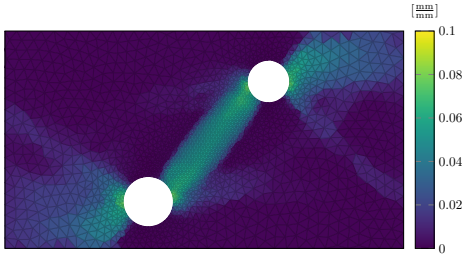

(c) Example of strain field (von Mises norm)

Figure 5 DIC mesh and kinematic fields examples

3.3 | Kinematic field extraction

3.3.1 | Kinematic measurement parameters

For this study, all the displacement fields $\mathbf{u}$ are obtained by DIC measurements based on the open-source library *Ufreckles* [28]. The optical flow is solved thanks to a Finite Element discretization of the sought displacement [29, 30]. Therefore, all measurements have an associated finite element mesh. For our application, the measurement is performed on an unstructured mesh of trianglar elements using a linear interpolation presented in Figure 5a. The mesh has been refined to an element size of 50 Pix in the area of strong strain gradients compared to a size of 150 Pix for the rest of the RoI. Two examples of displacement and strain fields are given in Figures 5b and 5c. A finite difference in time of the strains gives an estimate of the strain rate. All information regarding the DIC measurements and its post-processing is summarized in Table 2.

3.3.2 | Main kinematic features

Figure 6 presents the strain rate evolution during a specific time window of the test (between 1.75 and 4.25 s). This clearly illustrates the appearance of localized deformation zones. These localized bands are well known for this type of material and

correspond to Piobert–Lüders bands. The nucleation of the first band starts between the 2 holes and then it divides in two to propagate along the normal of the initial band. Other localization zones appear around the holes but are less visible than the central band and they do not involve the same deformation mechanisms at the microstructural scale of the material. The presence of localization bands and their interaction with the holes generate a complex local loading history despite a relatively simple macroscopic load.

3.4 | Initial stress solution

In this section, our main goal is to compute an initial solution close enough to the true stress field and thus improve the convergence of our algorithm. The stress field will be computed thanks to a simple material law, identified by a FEMU technique. As a reminder, FEMU methods, like other full-field identification methods, minimize the mismatch between the computed and experimental displacements [31, 3, 32, 9, 33] under equilibrium constraint. The main goal of this initial solution is to be quite close to the actual stress that the model-free algorithm aims at estimating. Therefore, the solution is computed using a prescribed loading. This is difficult as we only have access to the resultant of the forces and not to the local nodal force distribution. This difficulty is usually circumvented by invoking the St. Venant principle and imposing a uniform force distribution which here would be an oversimplification.

3.4.1 | Force profile on the boundary

To tackle this issue, we use a strategy similar to the one proposed in [9] to find a load profile on a boundary. From the DIC measurement and an initial guess of the constitutive parameters, a simulation is performed prescribing the measured displacement as boundary conditions along the top and bottom edges of the RoI, the left and right edges being stress free. The normal reaction force profiles $\mathbf{f}^{int}_{\partial\mathbf{u}}$ along the top boundary are extracted and corrected (applying an amplification factor) so that its integration along the boundary balances the external load exactly. The corrected profile is then reused in the identification algorithm as a prescribed nodal force distribution. All the remaining degrees of freedom on the boundaries are completed by prescribing the measured displacement. To summarize, the boundary conditions applied for FEMU along the RoI edges are the following:

- Left and right edge: stress free condition;
- Bottom edge: $\mathbf{u}_{DIC}$ along x and y is prescribed;
- Top edge: $\mathbf{u}_{DIC}$ along x and corrected force profile along y,

fig. 7 presents the boundary conditions used for the FEMU.

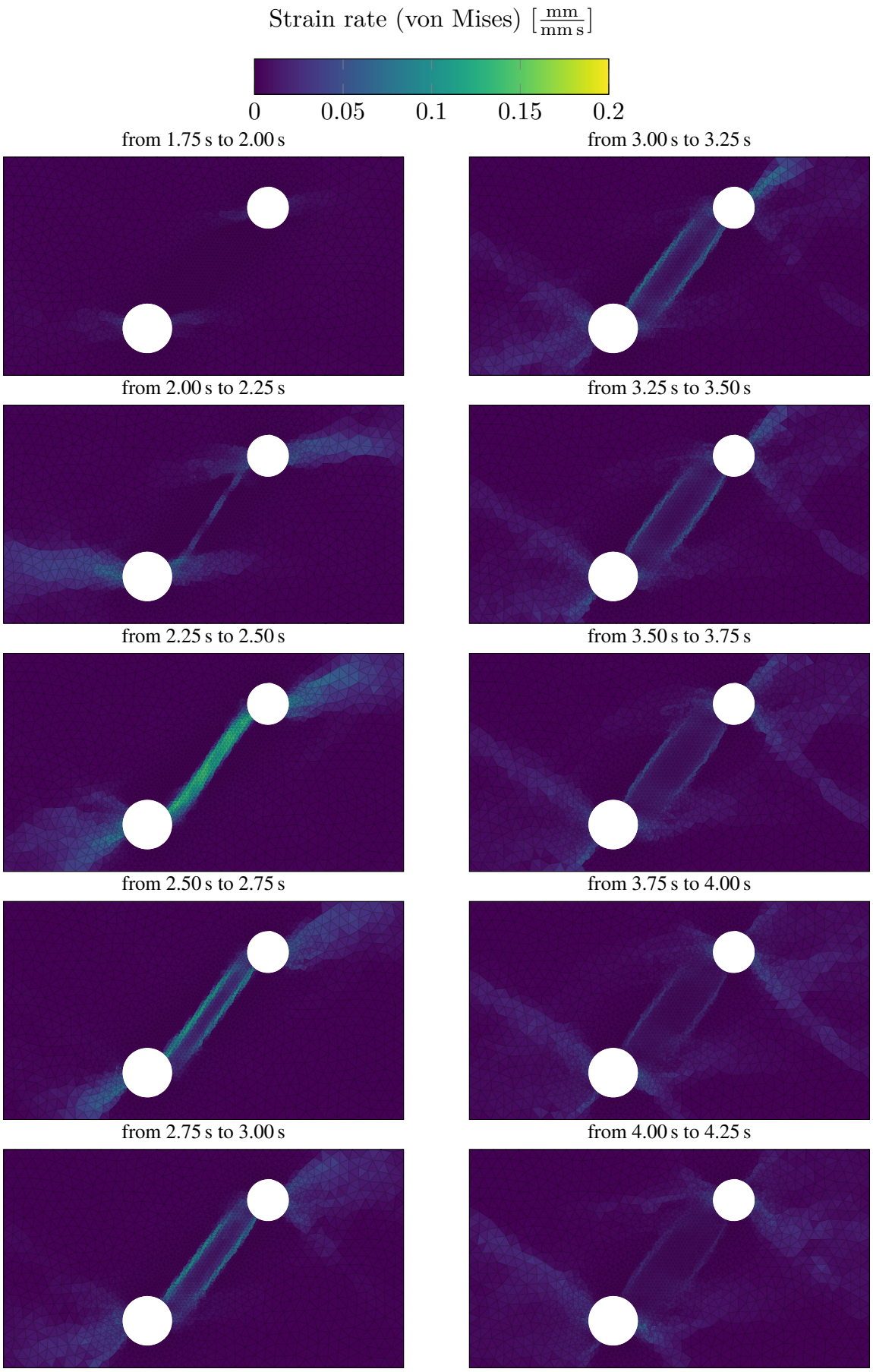

Figure 6 Strain rate $\dot{\varepsilon}$ evolution during the test (from left top to bottom then right top to bottom)

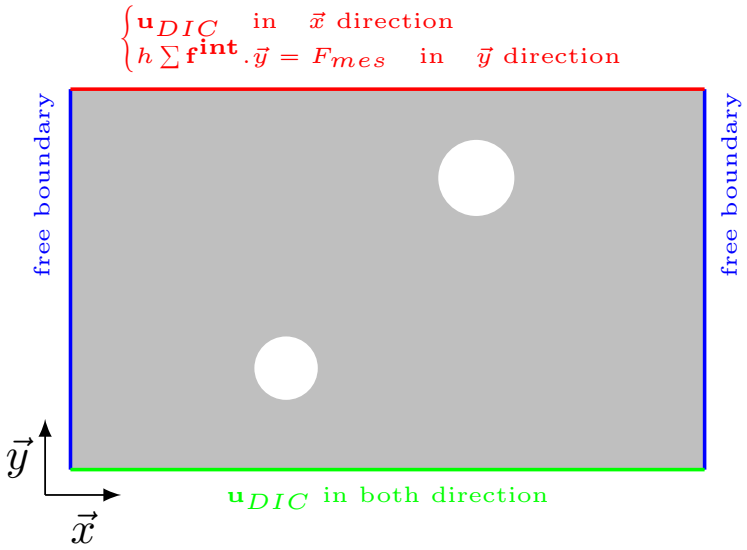

Figure 7 Boundary conditions used for the FEMU.

3.4.2 | Finite Element Model Updating

As discussed previously, the initialization of the stress field is performed using a usual and simple parametric law. The optimal material parameters of this law come from a FEMU scheme [32, 9]. The cost function minimized is built directly from the mismatch between measured and simulated displacements (respectively $\mathbf{u}_{DIC}$ and $\mathbf{u}_{FEM}$), and balancing the external forces. Once the optimal set of parameters is found, a final simulation is performed to obtain the initial optimal solution $(\boldsymbol{\sigma}^*_{FEMU}, \mathbf{u}^*_{FEMU})$ for the chosen constitutive equation.

3.4.3 | Constitutive modeling for the initial solution

The material model chosen is elasto-plastic with a linear kinematic hardening. Knowing the elastic parameters (that can be found in the literature), 2 other parameters have to be found: the yield stress $\boldsymbol{\sigma}_y$ and the hardening modulus H. As the loading always increases in the considered experiment, it would not have made any difference to choose a kinematic or an isotropic hardening. It is worth noting that standard linear hardening models are not suited to describe localization bands in metals. Elastic properties are assumed to be known, the value of Young's modulus is set to 240 GPa and the Poisson's ratio to 0.23. $\boldsymbol{\sigma}_y$ and H are initialized with these values: $\boldsymbol{\sigma}_y^{ini} = 300$ MPa and $H^{ini} = 1.4$ GPa. The optimized FEMU parameters are $\boldsymbol{\sigma}_y^{optim} = 322$ MPa and $H^{optim} = 1.21$ GPa.

3.5 | Kinematic mismatch and FEMU residual

Figure 8 presents the strain rate evolution over the red line defined on the mesh Figure 5a. This figure shows a significant mismatch in the kinematic fields between the model predictions and the measurements. While we observe peaks in the measured strain rates (Figure 8a), the elasto-plastic model predicts a smooth variation (Figure 8b).

In Figure 9, we plot the strain rate residual defined by Equation (21), the difference of the strain rate derived from the measurement $\mathbf{u}_{DIC}$ and the strain rate derived from the optimal parametric solution $\mathbf{u}^*_{FEMU}$:

$$\Delta\dot{\boldsymbol{\varepsilon}} = \frac{\partial}{\partial t}\left(\nabla^s \mathbf{u}_{DIC} - \nabla^s \mathbf{u}^*_{FEMU}\right). \tag{21}$$

Figure 9 clearly shows that the FEMU solution is unable to account for the localization of strain in the bands or around the holes.

In this example, the parametric solution smooths the strain rate variations of the Piober-Lüders bands. As expected, the simple elasto-plastic model is unable to reproduce a propagating shear band with the model acting as a low pass filter.

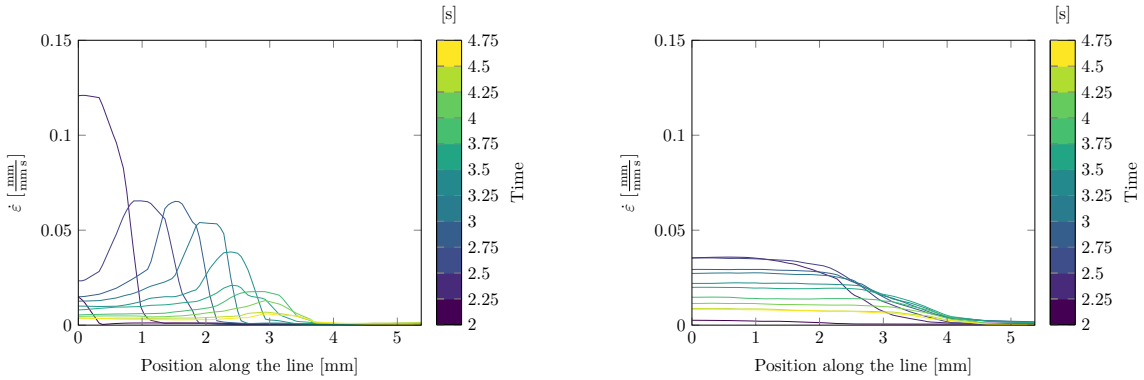

(a) Strain rate from $\mathbf{u}_{DIC}$ **(b)** Strain rate from $\mathbf{u}^*_{FEMU}$

Figure 8 Strain rate (von Mises) along the red line defined on Figure 5a

4 | PARAMETRIC STUDY

This section focuses on results regarding the proposed DDI methodology. Specifically, the choice of the correction basis and the integration weight p_e will be investigated. As changing the integration weight changes the norm used for evaluating the distance

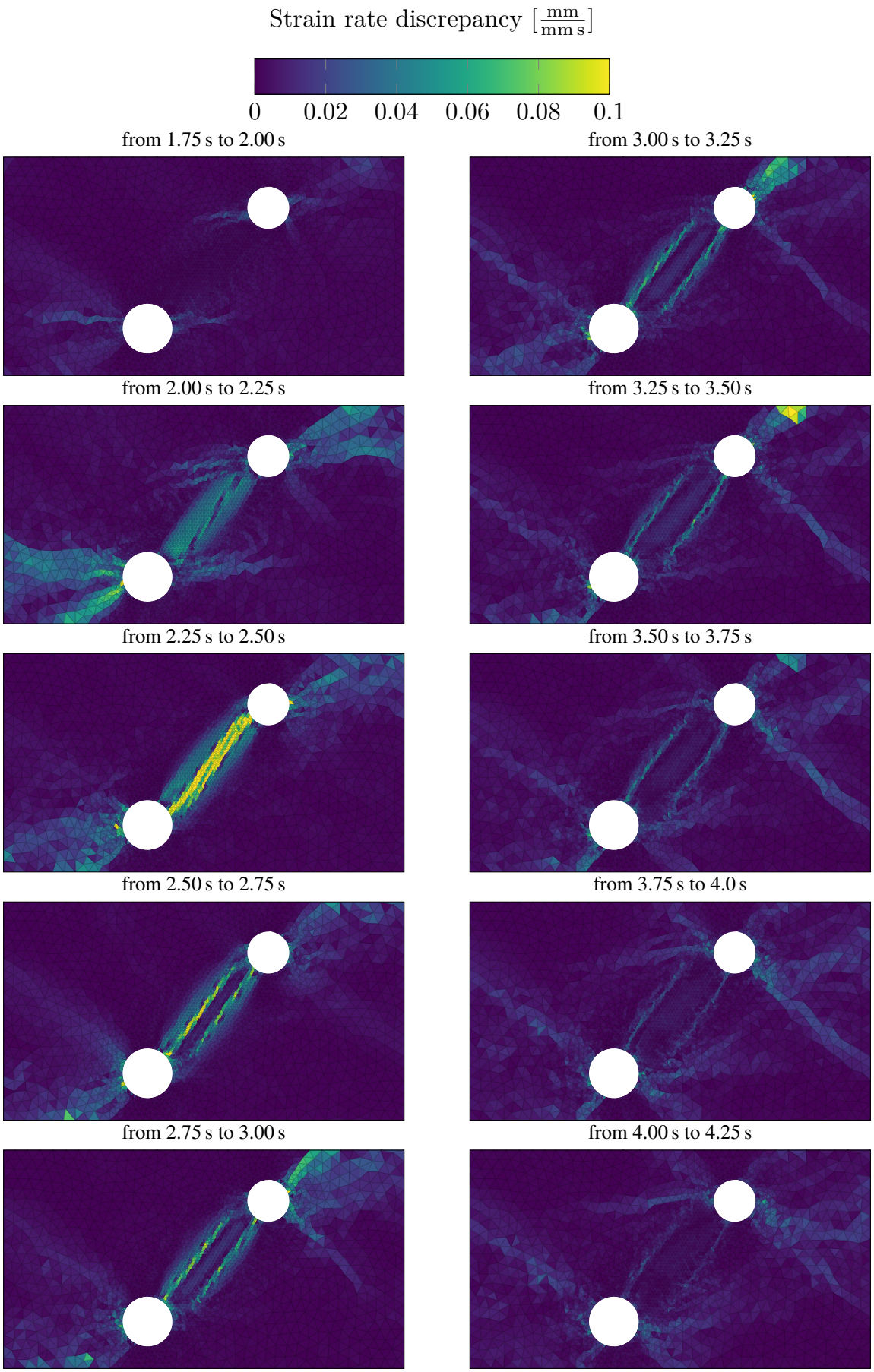

Figure 9 von Mises norm of strain rate residual $\Delta\dot{\boldsymbol{\epsilon}}$ Equation (21) (from left top to bottom then right top to bottom)

in the constitutive space, a one to one comparison of the results using different distances is not possible, so we introduce a different distance metric for comparison purposes:

$$\begin{aligned} \Phi &= \sum_{j=1}^{N_t} \sum_{e=1}^{N_e} \phi_e \\ \text{with,} \quad \phi_e &= \left| \sqrt{\mathbb{C}} : (\boldsymbol{\varepsilon}_e^j - \mathcal{S}_e^j \boldsymbol{\varepsilon}^*) \right| + \left| \left(\sqrt{\mathbb{C}} \right)^{-1} : (\boldsymbol{\sigma}_e^j - \mathcal{S}_e^j \boldsymbol{\sigma}^*) \right| \\ &+ \left| \sqrt{\mathbb{C}} : (\boldsymbol{\varepsilon}_e^{j-1} - \mathcal{S}_e^j \boldsymbol{\varepsilon}^{**}) \right| + \left| \left(\sqrt{\mathbb{C}} \right)^{-1} : (\boldsymbol{\sigma}_e^{j-1} - \mathcal{S}_e^j \boldsymbol{\sigma}^{**}) \right|. \end{aligned} \tag{22}$$

Φ is the space-time average L_1 norm and ϕ_e the local L_1 norm distance at element e. In the following, we will call the "Initial State" (and Initial Value) the correction-free solution. Meaning that the minimization is performed by searching only for the optimal material states and selection matrix, no correction to the stress field computed from FEMU is searched for.

4.1 | Influence of the stress correction basis $\mathbb{L}$ and the boundary conditions

Considering a constant value of the integration weight p_e of 1, we focus on the convergence of the DDI varying the type of correction basis (Boundary Condition 1 or 2 of section 2.1.4).

4.1.1 | L_1 norm, Φ

Figure 10 presents the algorithmic convergence using the L_1 norm Φ when correcting the Initial State. Table 3 presents the values of Φ and comparisons to the initial value Φ_{ini}.

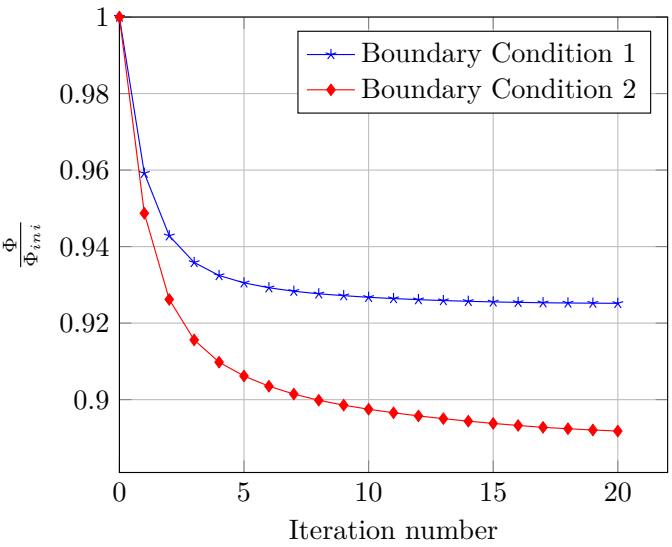

Figure 10 Effect of the stress correction basis $\mathbb{L}$ on the convergence using the L_1 norm, Φ

Boundary Condition type	1 - strong form	2 - weak form
Φ	8.755×10^7	8.439×10^7
$\frac{\Phi}{\Phi_{ini}}$	0.925	0.8918
$1 - \frac{\Phi}{\Phi_{ini}}[\%]$	7.48	10.82

Table 3 Values of Φ (normalized) at convergence

The final distance reached is significantly lower than for the Initial solution given thanks to the FEMU for the two considered types of boundary conditions. Both types of boundary conditions improve the distance Φ, but the weak form basis allows to reach a lower Φ. Boundary condition 2 actually allows the algorithm to explore a larger domain of the admissible stress space as the weak form is less constraining and the algorithm leads to a better consistency of the material states and the local states with the obtained stress fields.

4.2 | Impact of the Data-Driven integration weight

This part is dedicated to the effect of the Data-Driven integration weight p_e on the solution when the correction basis is the Boundary Condition 2 (as it allows to reach a better solution). The following values of the Data-Driven integration weight p_e are considered: $\frac{1}{w_e}$, 1 and w_e. As stated above, since p_e is assigned different values, Ψ is not suitable to compare the different solutions. Like in the previous section, the influence of p_e is thus studied with respect to Φ (eq. 22).

4.2.1 | Global convergence (L_1 norm, Φ)

We can see on Figure 11 the convergence of the method for the different weights p_e. Table 4 gives the values of Φ for the considered weights after the final update of $\mathcal{S}^t$.

p_e	w_e	1	$\frac{1}{w_e}$
Φ	8.5444×10^7	8.439×10^7	8.5843×10^7
$\frac{\Phi}{\Phi_{ini}}$	0.9029	0.8918	0.907
$1 - \frac{\Phi}{\Phi_{ini}}[\%]$	9.71	10.82	9.29

Table 4 Values of Φ after the final update of $\mathcal{S}^t$ (outside of the algorithm)

Different things have to be noted. First, regardless of the integration weight used, the final distance reached is significantly lower than for the Initial state given thanks to the FEMU. Second, using $p_e = 1$ seems to yield the best solution (with respect to the Φ norm) as it maximizes the difference to the Initial Value. Further, the convergence speed appears faster with the integration weight $p_e = 1$ which leads to a significantly lower value of the convergence indicator for a given number of iterations.

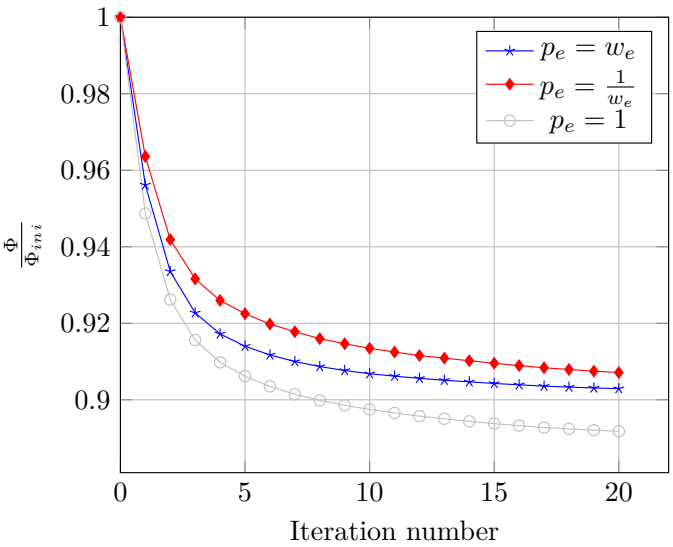

Figure 11 Effect of the integration weight p_e on the convergence using the L_1 norm, Φ

4.2.2 | Spatial distribution of the distance ϕ_e

To conclude on the effect of the integration weight, the spatial distribution of ϕ_e is investigated.

Figure 12 presents the local temporal average ($mean_t$) and standard deviation (std_t) of ϕ_e for all the considered integration weights relative to the Initial State. The average and the standard deviation show that the distribution is impacted by the value of the integration weight. Using $p_e = w_e$ allows to have a decrease of the relative distance for the large elements whereas using $p_e = w_e$ decreases it for the smaller ones. $p_e = 1$ is a good compromise between the two other cases but has a better temporal consistency which can explain that it reaches a smaller value for Φ as demonstrated in the previous paragraph.

5 | DATA-DRIVEN SOLUTION

We are finally interested in two outputs of the DDI, (i) the local states, (ii) the material states sampling the surface response in the constitutive space. First, we verify the static admissibility (balance of momentum and energetic balance) of the local state $(\boldsymbol{\varepsilon}_e, \boldsymbol{\sigma}_e)$. For the material states, a reduced representation using von Mises norm will be used to observe how the strain localization is accounted for. Finally, the identified local stress fields will be presented.

In the following paragraphs, we will analyse the fields resulting from a DDI algorithm computed with the weak form boundary condition (Boundary Condition 2) and with $p_e = 1$ as this setting gives the best solution given the criteria in Section 4.

5.1 | Mechanical analysis of the local states

In order to objectively characterize the mechanical fields (FEMU *v.s.* DDI), we propose to use two types of criteria to check the balance of the solutions in terms of stress and energy.

5.1.1 | Balance of the external load

The first criterion $\mathbf{r}(\boldsymbol{\sigma})$ is the relative difference between the internal forces $\mathbf{f}^{int}$ and the external forces $\mathbf{f}^{ext}$ vectors. It is used classically in computational inelasticity as a convergence criterion and is computed as follows:

$$\mathbf{r}(\boldsymbol{\sigma}, t) = \frac{\|\mathbf{f}^{ext}(\boldsymbol{\sigma}, t) - \mathbf{f}^{int}(\boldsymbol{\sigma}, t)\|_2}{\|F^t_{mes}\|_2}. \tag{23}$$

Here we use it to compute the balance between the applied load $\mathbf{f}^{ext}$ and the resulting internal forces of the considered stress states (FEMU and Data-Driven solutions). This criterion is also computed for the stress correction $\bar{\boldsymbol{\sigma}}$ to quantify the potential imbalance being introduced in the Initial FEMU state. For this purpose, we assume $\mathbf{f}^{ext}(\bar{\boldsymbol{\sigma}}) - \mathbf{f}^{int}(\bar{\boldsymbol{\sigma}}) = 0$ on the upper boundary of the RoI where a Neumann condition is considered.

Figure 13a presents the relative stress residual $\mathbf{r}$. The relative discrepancy between the applied load and the internal forces for both solutions is in the order magnitude of 10^{-4} meaning that they accurately balance the external load.Furthermore, the data-driven and parametric solutions are always superimposed. It is also clear that the correction is self-balanced, as the order of magnitude of the stress residual $\mathbf{r}$ is 10^{-9}.

5.1.2 | Energy balance

A second criterion is defined to check the energy balance of the solutions. This criterion $\mathbf{e}(\boldsymbol{\sigma}, t)$ defined by Equation (24) is based on the relative difference between the strain energy (for each available solution) and the *experimental* work of external forces evaluated from Figure 4. The estimation of the work of external forces is made under the assumption of equi-repartition of the force and the displacement along the edges. Thus $\mathbf{e}(\boldsymbol{\sigma}, t)$ gives only a superior bound of the relative energy discrepancy for the solutions,

$$\mathbf{e}(\boldsymbol{\sigma}, \mathbf{t}) = 1 - \frac{\int_0^t \mathbf{f}^{int}(\boldsymbol{\sigma}, \tau)\dot{\mathbf{u}}(\boldsymbol{\sigma}, \tau) d\tau}{\int_0^t F^\tau_{mes} \Delta \dot{U}^\tau_{RoI} d\tau}, \tag{24}$$

where the time integrals are estimated using a trapezoidal rule and the time derivatives with a finite difference scheme.

Figure 13b presents the evolution of $\mathbf{e}(\boldsymbol{\sigma}, \mathbf{t})$ criterion for both solutions (FEMU and DDI). The relative energy residual for the FEMU solution is always greater in absolute value than the DDI solution at the beginning and during the nucleation/propagation of the localization bands. By the end of the considered time interval, the FEMU solution reaches values similar to the DDI

ones. The value of $\mathbf{e}(\boldsymbol{\sigma}_{DDI}, t)$ remains closer to zero for all time steps. This mostly comes from the kinematic discrepancy in the FEMU solution (the displacement field obtained by FEMU does not match with the measured one) which is at its maximum during the main localization event and decreases afterwards.

5.2 | Material states coverage of the constitutive space

Figures 14a and 14b present the sampling of the material response by the material states $(\boldsymbol{\varepsilon}^*, \boldsymbol{\varepsilon}^{**}, \boldsymbol{\sigma}^*, \boldsymbol{\sigma}^{**})$ on a reduced space $(\boldsymbol{\varepsilon}^*, \boldsymbol{\varepsilon}^* - \boldsymbol{\varepsilon}^{**}, \boldsymbol{\sigma}^*)$ and using the von Mises norm for these tensors. Note that $\boldsymbol{\varepsilon}^* - \boldsymbol{\varepsilon}^{**}$ can be considered as a pseudo-strain rate.

We can clearly see that for a constant stress at the beginning of the non-elastic stress-strain relation, there is an important variation of the pseudo-strain rate which is consistent with how Piobert–Lüders bands are classically encountered in uniaxial tests. Without any assumption on the mathematical formula describing the constitutive relation, a linear relation between stress and strain, which could be interpreted as linear hardening, is observed after the elastic regime and for low strain rate. Conversely, it appears that the yield stress remains constant for higher strain rates (within the bands). This kind of Piobert–Lüders plateau is consistent with the results obtained in the literature for uniaxial tests.

5.3 | Identified stress fields

Figure 15 presents the evolution of the stress obtained by DDI. We can clearly see a concentration of the stress around the holes and between them as the load increases. To further analyzes these stress field and their evolution, Figure 16 presents the evolution of the first invariant of stress rate $I_1(\dot{\boldsymbol{\sigma}})$ compared to the evolution of the strain rate (von Mises norm).

The stress rate shows release peaks or valleys (decreases of the considered quantity) similar to the intensification peaks observed on the strain rate in Figures 6 and 8a. However, the stress rate valleys are ahead (in advance considering the propagation of the strain rate band) of the strain rate peaks. This means that a stress release is identified ahead of the propagating strain localization band. This effect is visible for all time steps presented in Figure 8a. However, it is clearly observed at instants when the band position changes and its intensity is significant. When the band intensity diminishes, resulting in a low signal to noise ratio (on the strain rate), observing the stress localization ahead of the strain becomes more difficult. Therefore only the time steps when the phenomenon is clearly visible are presented.

Again we can clearly see in **??**, that the local stress history is quite complex with a negative stress rate indicating a local unloading of the material despite a monotonous macroscopic load.

6 | DISCUSSION AND PERSPECTIVES

In this work, an extension of the Data-Driven Identification method [16] to history dependent materials is proposed. A study of the influence of some parameters (namely the integration weight and boundary condtions treatment) of the method is presented and supplements the one proposed in [19]. From this, optimal parameters are obtained and used to identify stress fields that are compared using two criteria to a classical parametric solution using Finite Element Model Updating, used to initialize the DDI problem.

This method allows to estimate the local stresses in highly unfavorable settings such as non homogeneous experiments involving strain gradient and strain rate localization. The material states identified (which sample the material response in the considered constitutive space) also exhibit the expected properties of a Piobert–Lüders plateau. The estimated stress-strain pairs are more consistent from an energetic standpoint compared to the parametric solution with a still simple description of the behavior.

A few issues should be highlighted, the current method has been written for evanescent memory materials so the formulation might not be suitable for highly viscous solids, but the formulation could be modified to take into account more time steps and therefore longer time interaction between stress and strain. Furthermore, as stated in [22], increasing the order of derivative should lead to more refined descriptions of the behavior.

It should also be mentioned that the impact of the DDI integration weight being relatively small, the choice of p_e could be tailored to a specific phenomenon. A spatially varying integration weight could also be used. For instance, for highly local phenomena such as cracks, the use of $p_e = \frac{1}{w_e}$ might be suited to ensure a stronger consistency of the local states with respect to the material states close to the crack tip .

Finally, from the non-parametric identified stress and by adding some assumptions: (1) additive partition of the elastic and plastic strain, (2) J_2 plasticity (von Mises) and (3) plane stress hypotheses, it is possible to reconstruct the full stress and strain tensors (including out of plane components) and to compute some internal variables such as the plastic strain. Figure 17 presents the von Mises norm of the plastic strain rate (or the cumulative plasticity rate) during the nucleation and propagation of the localization band. This evolution of the plastic strain is consistent with Figures 6 and 16 and allows to interpret the variation of the first invariant of the stress rate as an elastic distortion for accommodating the propagation of the band. It clearly shows that by adding *a posteriori* some modelling hypotheses, the method allows to recover the kinematic of an anelastic band in a sample submitted to non-homogeneous states. This offers the opportunity to take even greater advantage of the proposed method for investigating behaviours that are difficult to capture using constitutive equations usually defined based on uniaxial experimental data.

Using this method coupled with other experimental characterization methods like Infrared Thermography could allow a complete description of the local dissipation and could give us more insights on the local behavior of materials under complex loading. 3D X-Ray Tomography and DVC should allow the evaluation of a 3D stress tensor and its spatial variation within the bulk of a sample.

References

[1] M. Grédiac, F. Sur, and B. Blaysat. "The Grid Method for In-plane Displacement and Strain Measurement: A Review and Analysis". In: *Strain* 52.3 (May 2016), pp. 205–243. DOI: 10.1111/str.12182. eprint: https://onlinelibrary.wiley.com/doi/pdf/10.1111/str.12182.

[2] M. A. Sutton, J-J. Orteu, and H. W. Schreier. "Digital Image Correlation (DIC)". In: *Image Correlation for Shape, Motion and Deformation Measurements*. Boston, MA: Springer US, 2009, pp. 1–37. ISBN: 978-0-387-78747-3. DOI: 10.1007/978-0-387-78747-3_5.

[3] S. Avril et al. "Overview of Identification Methods of Mechanical Parameters Based on Full-field Measurements". en. In: *Exp Mech* 48.4 (July 2008), p. 381. ISSN: 1741-2765. DOI: 10.1007/s11340-008-9148-y.

[4] J.-C. Passieux et al. "Multiscale Displacement Field Measurement Using Digital Image Correlation: Application to the Identification of Elastic Properties". In: *Exp Mech* 55.1 (Jan. 2015), pp. 121–137. ISSN: 0014-4851, 1741-2765. DOI: 10.1007/s11340-014-9872-4.

[5] P. Leplay et al. "Damage law identification of a quasi brittle ceramic from a bending test using Digital Image Correlation". In: *Journal of the European Ceramic Society* 30.13 (Oct. 2010), pp. 2715–2725. ISSN: 0955-2219. DOI: 10.1016/j.jeurceramsoc.2010.05.021.

[6] B. Blaysat et al. "A Dissipation Gap Method for full-field measurement-based identification of elasto-plastic material parameters". In: *Int. J. Numer. Meth. Engng* 91.7 (Aug. 17, 2012), pp. 685–704. ISSN: 00000003. DOI: 10.1002/nme.4287.

[7] L. Crouzeix et al. "An orthotropic variant of the equilibrium gap method applied to the analysis of a biaxial test on a composite material". In: *Composites Part A: Applied Science and Manufacturing* 40.11 (Nov. 1, 2009), pp. 1732–1740. ISSN: 1359-835X. DOI: 10.1016/j.compositesa.2009.08.016.

[8] M. Bertin, F. Hild, and S. Roux. "On the identifiability of Hill-1948 plasticity model with a single biaxial test on very thin sheet". In: *Strain* 53.5 (2017). _eprint: https://onlinelibrary.wiley.com/doi/pdf/10.1111/str.12233, e12233. ISSN: 1475-1305. DOI: 10.1111/str.12233.

[9] J. Réthoré et al. “Robust identification of elasto-plastic constitutive law parameters from digital images using 3D kinematics”. en. In: *International Journal of Solids and Structures* 50.1 (Jan. 2013), pp. 73–85. ISSN: 0020-7683. DOI: 10.1016/j.ijsolstr.2012.09.002.

[10] J. Neggers et al. “Improving full-field identification using progressive model enrichments”. In: *International Journal of Solids and Structures* 118-119 (July 1, 2017), pp. 213–223. ISSN: 0020-7683. DOI: 10.1016/j.ijsolstr.2017.03.013.

[11] R. Seghir and F. Pierron. “A Novel Image-based Ultrasonic Test to Map Material Mechanical Properties at High Strain-rates”. In: *Exp Mech* 58.2 (Feb. 1, 2018), pp. 183–206. ISSN: 0014-4851, 1741-2765. DOI: 10.1007/s11340-017-0329-4.

[12] L. Fletcher and F. Pierron. “The Image-Based Inertial Release (IBIR) Test: A New High Strain Rate Test for Stiffness Strain-Rate Sensitivity Identification”. In: *Exp Mech* 60.4 (Apr. 2020), pp. 493–508. ISSN: 0014-4851, 1741-2765. DOI: 10.1007/s11340-019-00580-6.

[13] C. Liu. “Nonuniform Stress Field Determination Based on Deformation Measurement”. In: *Journal of Applied Mechanics* 88.7 (July 1, 2021), p. 071005. ISSN: 0021-8936, 1528-9036. DOI: 10.1115/1.4050535.

[14] B. Cameron and C. Tasan. “Full-field stress computation from measured deformation fields: A hyperbolic formulation”. In: *Journal of the Mechanics and Physics of Solids* 147 (Feb. 1, 2021), p. 104186. ISSN: 0022-5096. DOI: 10.1016/j.jmps.2020.104186.

[15] A. Leygue et al. “Data-based derivation of material response”. In: *Computer Methods in Applied Mechanics and Engineering* 331 (Apr. 2018), pp. 184–196. ISSN: 0045-7825. DOI: 10.1016/j.cma.2017.11.013.

[16] A. Leygue et al. “Non-parametric material state field extraction from full field measurements”. en. In: *Comput Mech* 64.2 (Aug. 2019), pp. 501–509. ISSN: 1432-0924. DOI: 10.1007/s00466-019-01725-z.

[17] T. Kirchdoerfer and M. Ortiz. “Data-driven computational mechanics”. In: *Computer Methods in Applied Mechanics and Engineering* 304 (June 2016), pp. 81–101. ISSN: 0045-7825. DOI: 10.1016/j.cma.2016.02.001.

[18] T. Kirchdoerfer and M. Ortiz. “Data Driven Computing with noisy material data sets”. In: *Computer Methods in Applied Mechanics and Engineering* 326 (Nov. 2017), pp. 622–641. ISSN: 0045-7825. DOI: 10.1016/j.cma.2017.07.039.

[19] M. Dalémat et al. “Measuring stress field without constitutive equation”. en. In: *Mechanics of Materials* 136 (Sept. 2019), p. 103087. ISSN: 0167-6636. DOI: 10.1016/j.mechmat.2019.103087.

[20] P. Ladevèze, D. Néron, and P-W. Gerbaud. “Data-driven computation for history-dependent materials”. en. In: *Comptes Rendus Mécanique*. Data-Based Engineering Science and Technology 347.11 (Nov. 2019), pp. 831–844. ISSN: 1631-0721. DOI: 10.1016/j.crme.2019.11.008.

[21] F. Chinesta et al. “Data-Driven Computational Plasticity”. en. In: *Procedia Engineering*. International Conference on the Technology of Plasticity, ICTP 2017, 17-22 September 2017, Cambridge, United Kingdom 207 (Jan. 2017), pp. 209–214. ISSN: 1877-7058. DOI: 10.1016/j.proeng.2017.10.763.

[22] R. Eggersmann et al. “Model-Free Data-Driven inelasticity”. en. In: *Computer Methods in Applied Mechanics and Engineering* 350 (June 2019), pp. 81–99. ISSN: 0045-7825. DOI: 10.1016/j.cma.2019.02.016.

[23] L. Stainier, A. Leygue, and M. Ortiz. “Model-free data-driven methods in mechanics: material data identification and solvers”. en. In: *Comput Mech* 64.2 (Aug. 2019), pp. 381–393. ISSN: 1432-0924. DOI: 10.1007/s00466-019-01731-1.

[24] J. MacQueen. “Some methods for classification and analysis of multivariate observations”. In: *Proceedings of the Fifth Berkeley Symposium on Mathematical Statistics and Probability, Volume 1: Statistics* 5.1 (Jan. 1, 1967). Publisher: University of California Press, pp. 281–298.

[25] D. Arthur and S. Vassilvitskii. *k-means++: The Advantages of Careful Seeding*. Technical Report 2006-13. Stanford InfoLab, June 2006.

[26] M. Dalémat et al. “Reliability of the Data-Driven Identification algorithm with respect to incomplete input data”. In: *Constitutive Models for Rubber XI*. CRC Press, June 2019, pp. 311–316. DOI: 10.1201/9780429324710-55.

[27] M. Dalémat et al. “Robustness of the Data-Driven Identification algorithm with incomplete input data”. working paper or preprint. June 2021.

[28] J. Réthoré. *UFreckles*. 2018. DOI: 10.5281/zenodo.1433776.

[29] Y. Sun et al. “Finite element formulation for a digital image correlation method”. EN. In: *Appl. Opt., AO* 44.34 (Dec. 2005). Publisher: Optical Society of America, pp. 7357–7363. ISSN: 2155-3165. DOI: 10.1364/AO.44.007357.

[30] G. Besnard, F. Hild, and S. Roux. ““Finite-Element” Displacement Fields Analysis from Digital Images: Application to Portevin–Le Châtelier Bands”. en. In: *Exp Mech* 46.6 (Dec. 2006), pp. 789–803. ISSN: 1741-2765. DOI: 10.1007/s11340-006-9824-8.

[31] F. Hild and S. Roux. “Digital Image Correlation: from Displacement Measurement to Identification of Elastic Properties – a Review”. en. In: *Strain* 42.2 (May 2006). _eprint: https://onlinelibrary.wiley.com/doi/pdf/10.1111/j.1475-1305.2006.00258.x, pp. 69–80. ISSN: 1475-1305. DOI: 10.1111/j.1475-1305.2006.00258.x.

[32] J. Réthoré. “A fully integrated noise robust strategy for the identification of constitutive laws from digital images”. en. In: *International Journal for Numerical Methods in Engineering* 84.6 (Apr. 2010). _eprint: https://onlinelibrary.wiley.com/doi/pdf/10.1002/nme.2908, pp. 631–660. ISSN: 1097-0207. DOI: 10.1002/nme.2908.

[33] S. Roux and F. Hild. “Optimal procedure for the identification of constitutive parameters from experimentally measured displacement fields”. en. In: *International Journal of Solids and Structures*. Physics and Mechanics of Random Structures: From Morphology to Material Properties 184 (Feb. 2020), pp. 14–23. ISSN: 0020-7683. DOI: 10.1016/j.ijsolstr.2018.11.008.

□

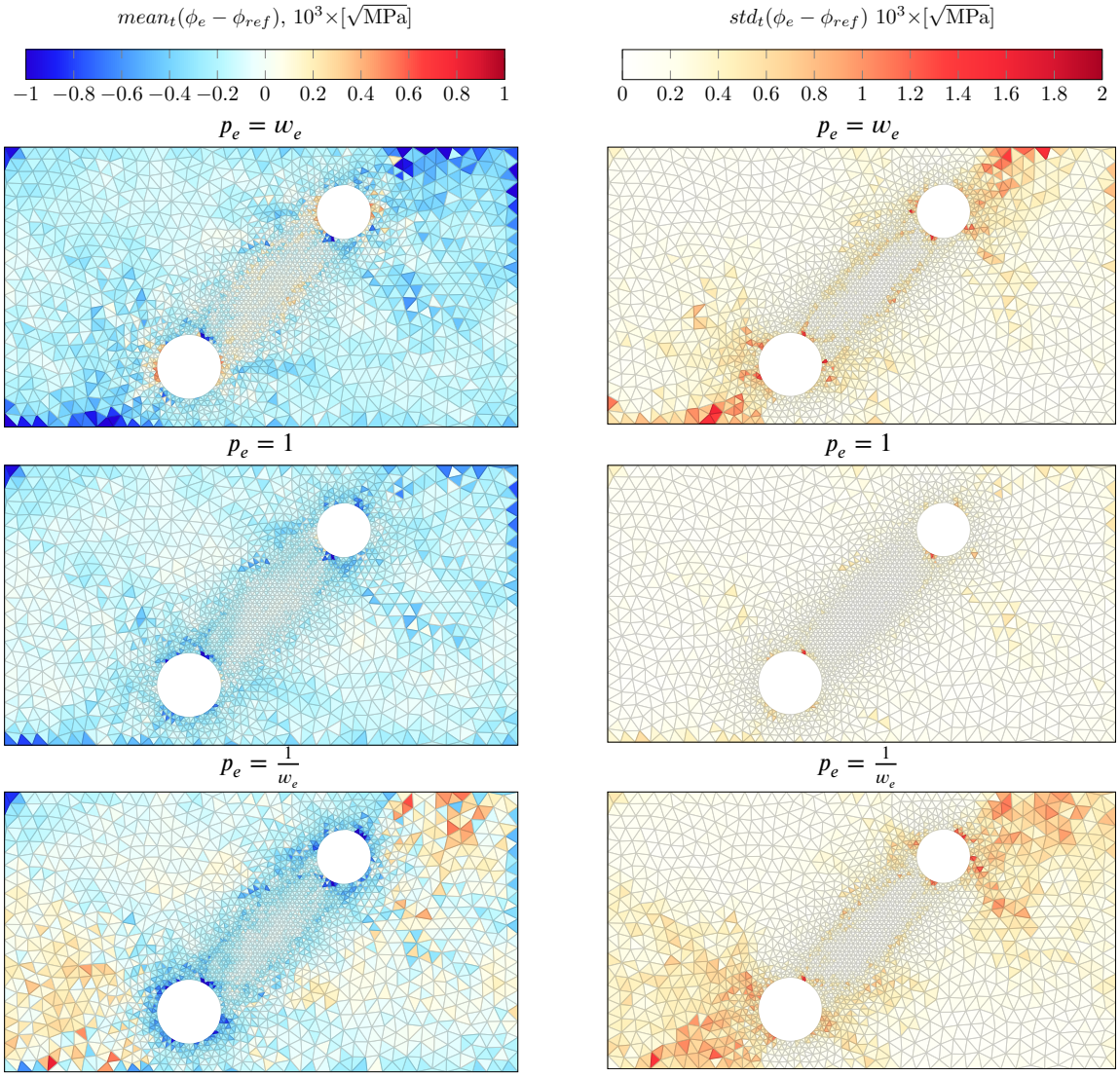

Figure 12 Spatial distribution of the ϕ_e

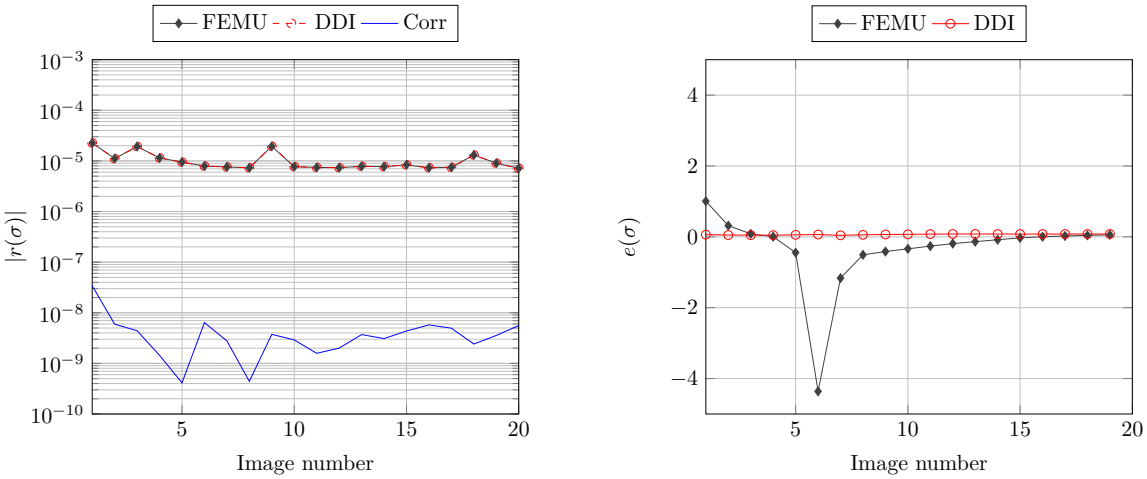

(a) Relative stress residual

(b) Relative strain energy residual

Figure 13 Criteria for the FEMU solution and DDI solution

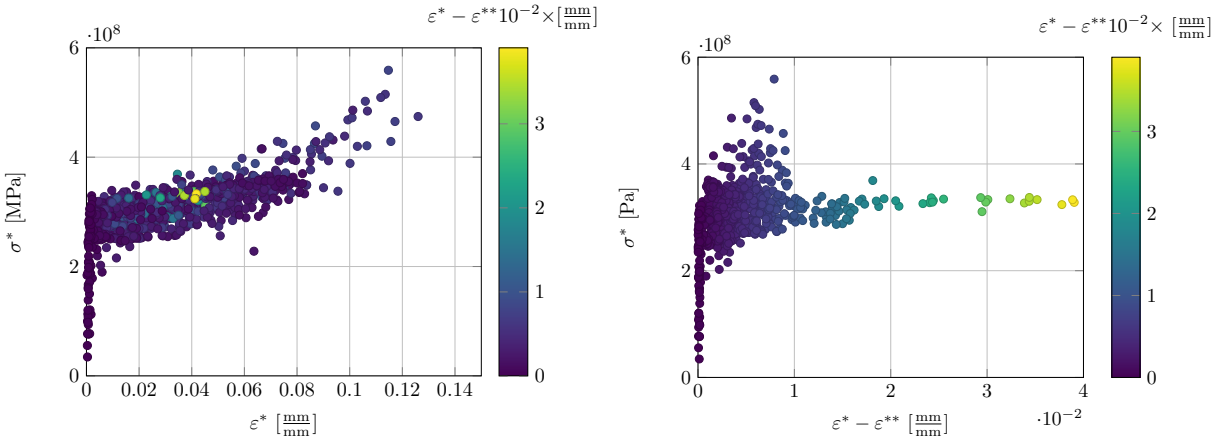

(a) Stress-Strain

(b) Stress-Strain Rate

Figure 14 Material state (von Mises norm) in a reduced constitutive space $(\boldsymbol{\varepsilon}^*, \boldsymbol{\varepsilon}^* - \boldsymbol{\varepsilon}^{**}, \boldsymbol{\sigma}^*)$, with $\boldsymbol{\varepsilon}^* - \boldsymbol{\varepsilon}^{**}$ a dimensionless strain rate. The material states capture variations of the strain rate for a constant stress is a known marker of Piobert–Lüders band.

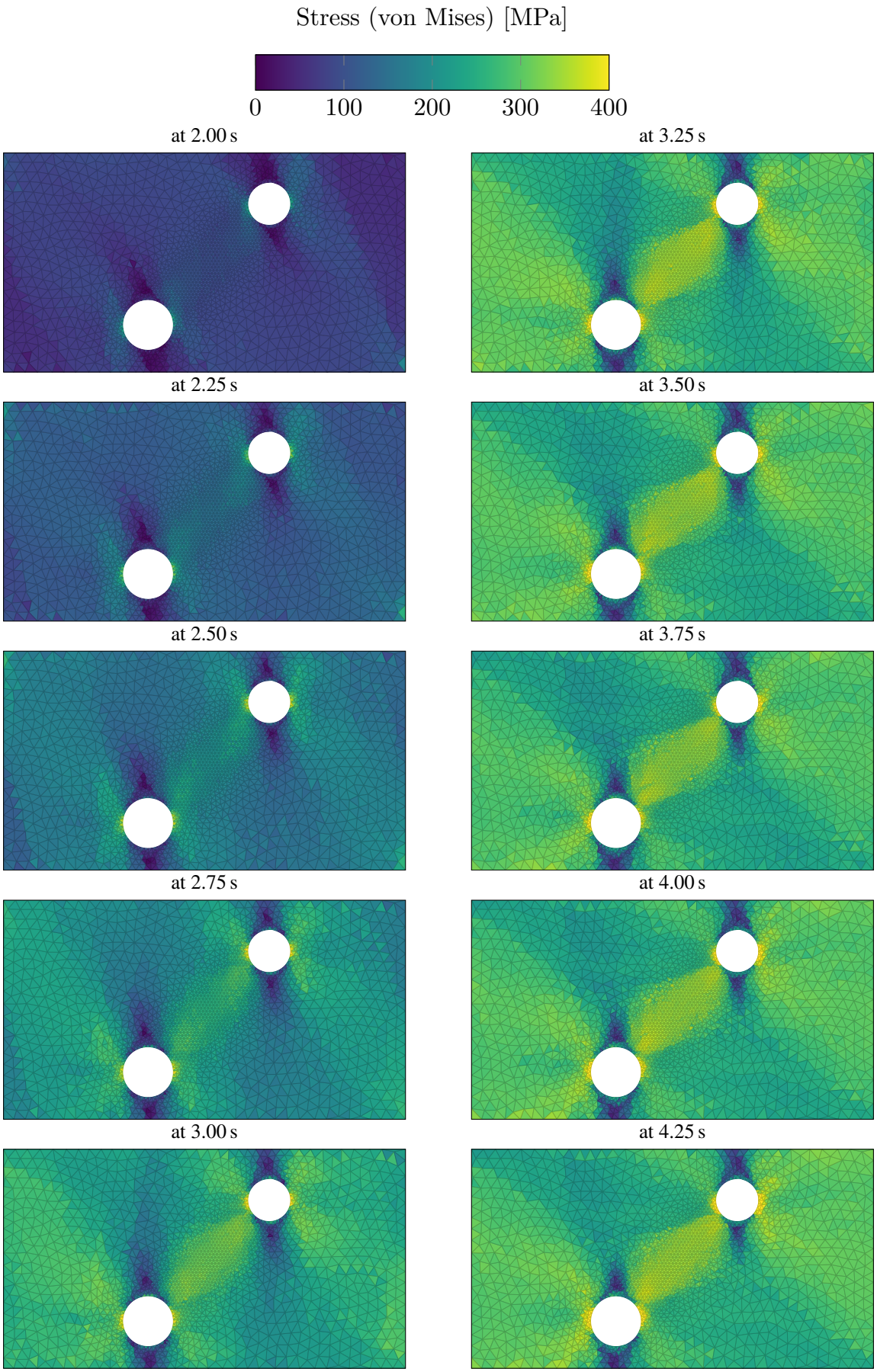

Figure 15 DDI stress field evolution during the test (from left top to bottom then right top to bottom)

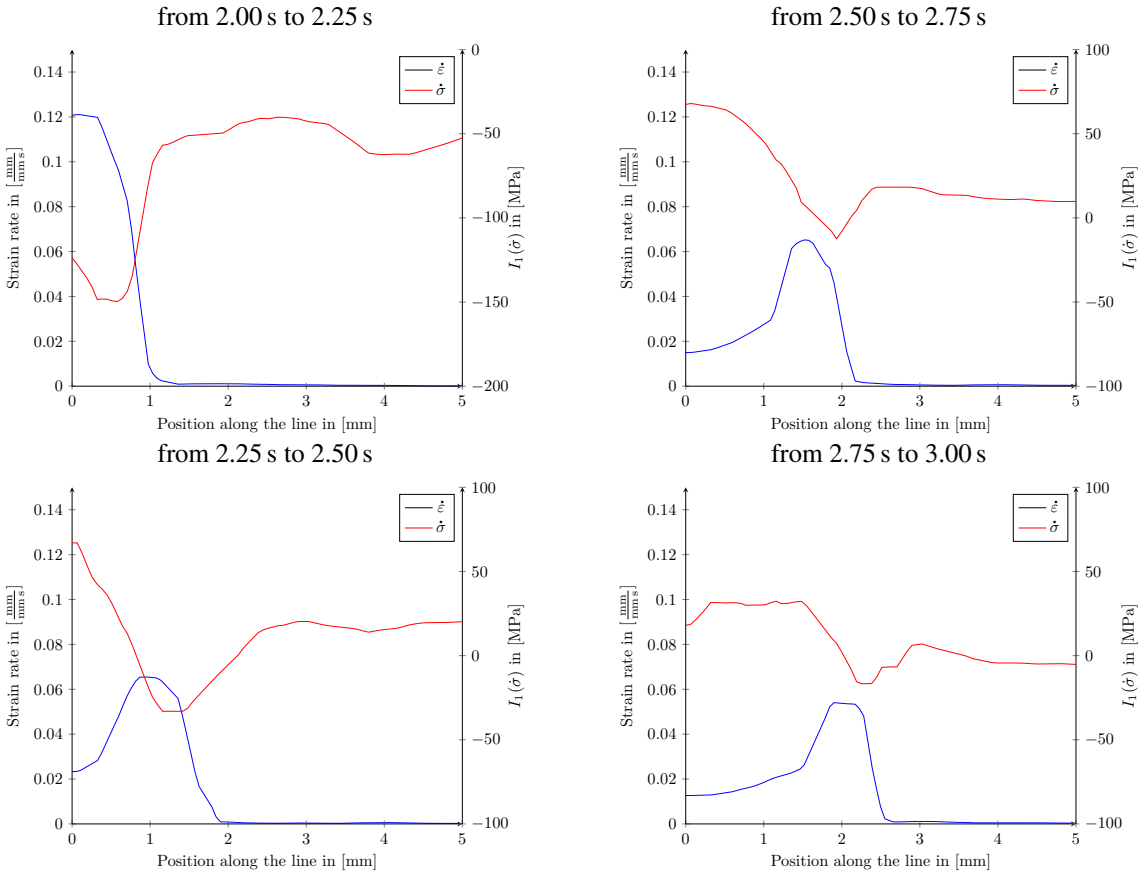

Figure 16 Comparison of the stress rate (first invariant) and strain rate (von Mises norm) profiles along the line defined on Figure 5a

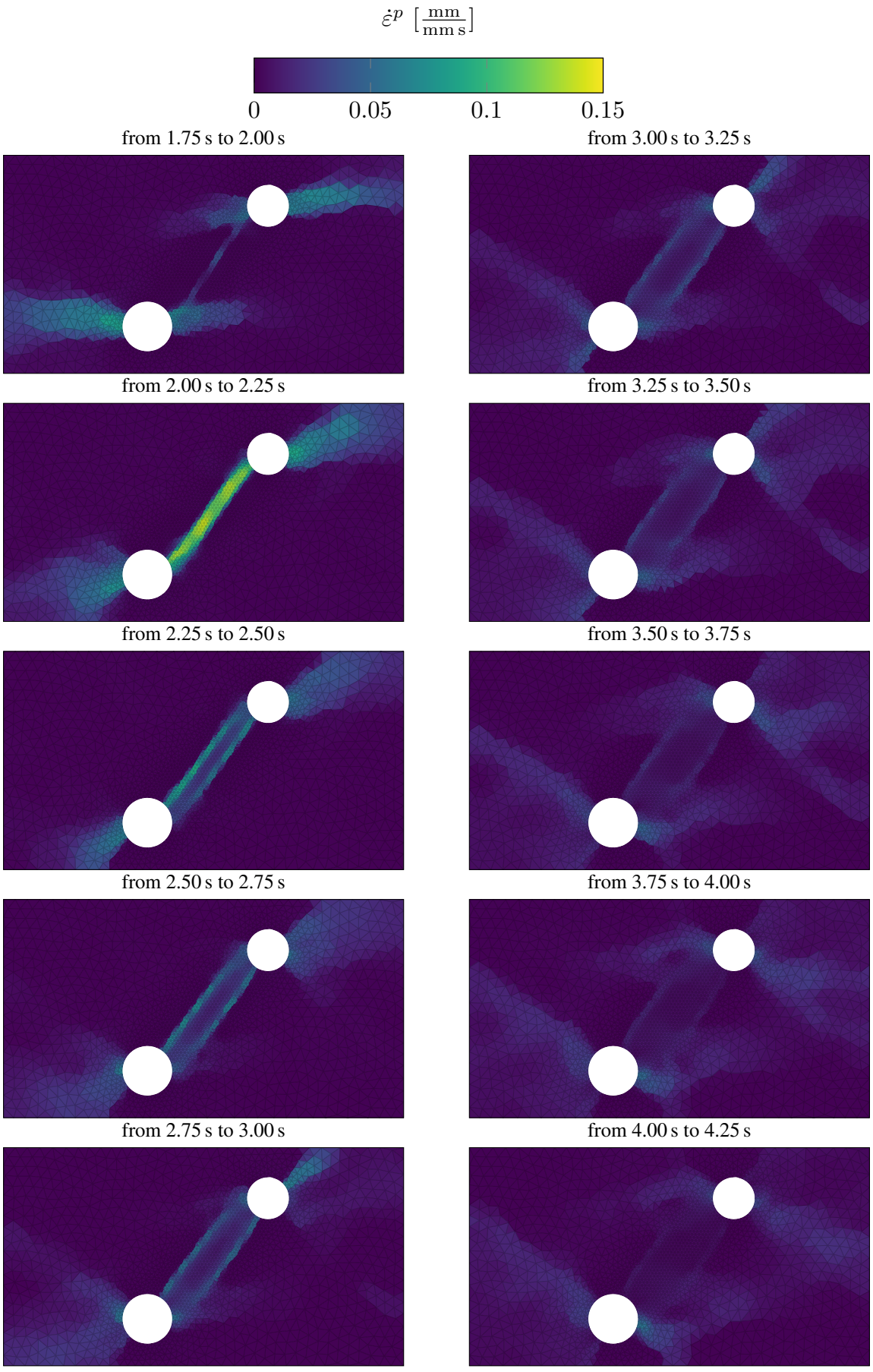

Figure 17 Anelastic strain rate evolution during the test